


## Article

# Assistance to Determine the Stability State of a Reactive Sputtering Process Based on the Analytical Solution of the Classical Berg Model

Marcell Gajdics <sup>1,2,\*</sup>, Nikolett Hegedűs <sup>3</sup>, Dániel Olasz <sup>1,2</sup> and Miklós Serényi <sup>1</sup> 

<sup>1</sup> Institute for Technical Physics and Materials Science, HUN-REN Centre for Energy Research, H-1121 Budapest, Hungary

<sup>2</sup> Department of Materials Physics, Eötvös Loránd University, ELTE, Pázmány Péter sétány 1/A, H-1117 Budapest, Hungary

<sup>3</sup> Guardian Orosháza Ltd., Csorvási u. 31, H-5900 Orosháza, Hungary

\* Correspondence: gajdics.marcell@ek.hun-ren.hu

**Abstract:** In this study, we propose simple analytical formulas for reactive sputtering technology, which can be used to assist in the selection of appropriate sputtering parameters during the deposition of thin films. Radio frequency (RF) sputtered alumina (Al<sub>2</sub>O<sub>3</sub>) was used to evaluate the results. Layers with O/Al ratios ranging from 24/76 to 54/73 were deposited. Following effective deposition, the equations of the Berg model describing the process were studied. The achieved stoichiometry and the associated technological parameters are of critical importance for the analysis of the equations; consequently, this established the primary guiding principle when selecting the analytical approximations. A straightforward graph of the processing parameters (pumping speed, partial pressure) has been constructed, with the objective of avoiding the hysteresis that is an inherent feature of the reactive sputtering process. In addition, we have extended the classical Berg model to examine how the biased substrate can influence deposition. It was found that applying a substrate bias can decrease target coverage, while it does not alter substrate coverage.

**Keywords:** Berg model; reactive sputtering; bias



Academic Editor: Panos Pouloupoulos

Received: 28 March 2025

Revised: 15 April 2025

Accepted: 20 April 2025

Published: 22 April 2025

**Citation:** Gajdics, M.; Hegedűs, N.; Olasz, D.; Serényi, M. Assistance to Determine the Stability State of a Reactive Sputtering Process Based on the Analytical Solution of the Classical Berg Model. *Coatings* **2025**, *15*, 499. <https://doi.org/10.3390/coatings15050499>

**Copyright:** © 2025 by the authors. Licensee MDPI, Basel, Switzerland. This article is an open access article distributed under the terms and conditions of the Creative Commons Attribution (CC BY) license (<https://creativecommons.org/licenses/by/4.0/>).

## 1. Introduction

The hysteresis effect characteristic of reactive sputtering is a well-known problem [1]. The original Berg model was the first to model it reliably [2]. Numerous articles have already been published based on this research, and the influence of material and process parameters on the development of hysteresis can be vividly demonstrated through numerical evaluation [3–5]. However, as demonstrated by [6,7], the model is not entirely accurate in its description. The main reason is that not all processes of target oxidation were included. Later, the Berg model was extended to incorporate these processes, designated as the upgraded Berg model [4].

Beyond its theoretical significance, however, from a practical point of view, it is important to ensure the stability of the reactive sputtering technological process [6,8,9]. The switching of the process from the metallic mode to the poisoned mode (or vice versa) is induced by a change in the reactive gas pressure. Due to the change in the coverage of the target with oxide, there is a change in the discharge current, as well [10]. The system reaches another equilibrium, which is not necessarily favorable from the point of view of the desired layer stoichiometry. By using direct or automated feedback control or superimposed low-frequency pulses, the deposition process can be stabilized [9,11,12].

In this study, aluminum oxide was used as a model material for the study of the reactive sputtering process.  $\text{Al}_2\text{O}_3$  (alumina) was chosen because it is the only oxide of Al; in addition, aluminum oxide thin films are widely used in many integrated optical and microelectronic applications due to their excellent mechanical, insulating, and optical properties. For example, low-loss optical guiding layers were demonstrated recently [13]. Therefore, the literature is abundant with studies on its reactive sputtering process. There are many descriptions of its deposition by DC or RF magnetron sputtering and comprehensive investigations on the physical properties (e.g., composition, refractive index) of the deposited layer [13–16].

Although there are numerical calculations to analyze the reactive sputtering process, in this study, we chose an analytical approach. Our aim was to provide relatively simple formulas to determine the stability state of a sputtering system. We compare the numerical and the reasonable approximate analytical calculations describing the reactive sputtering process based on the classical Berg equations. With the help of these evaluation procedures, a stability state diagram is presented. We also investigated the effect of the negative bias voltage applied to the substrate on discharge current vs. target voltage characteristics. Based on this, we extended the Berg equations to include the effect of substrate bias, which, to the best of our knowledge, has not been attempted before.

## 2. Materials and Methods

A LEYBOLD (Cologne, Germany) Z400 RF sputtering device was used to sputter a 99.999% pure Al target (diameter: 3"). The vacuum chamber was equipped with a turbomolecular pump (LEYBOLD (Cologne, Germany) Turbovac 450 iX) with a nominal maximal pumping speed of 450 L/s. The effective pumping speed (which also takes into account the conductance of the vacuum chamber) for oxygen was determined before the sputtering experiments by measuring the pressure change as a result of changing the oxygen flow rate regulated by a flow controller. Thus, the effective pumping speed was calculated to be 256 L/s. The rotation speed of the pump, as a consequence the pumping speed, can also be adjusted. The target–substrate distance was about 5 cm during sputtering, which took place in a vacuum chamber with a base pressure no higher than  $3 \times 10^{-4}$  Pa. The pressure was measured using a built-in LEYBOLD (Cologne, Germany) Penningvac PTR 90 vacuum gauge. Oxygen gas flow was controlled using an EL-FLOW Prestige mass flow meter (Bronkhorst High-Tech B.V., Ruurlo, The Netherlands), while the Ar working gas was regulated using a needle valve.

Sputtering of the alumina layers was performed using a constant discharge current density of  $27.95 \text{ A/m}^2$ , while the oxygen flow was varied. The total pressure was 0.7 Pa for all deposition experiments. Si single crystals were used as the substrate material.

An Advanced Energy Caesar type RF generator with a frequency of 13.56 MHz was used to provide a constant power of up to 500 W, which was coupled to the target through a  $50 \Omega$  matching circuit. The DC target voltage—generated on the target due to the rectifying effect of the plasma—was measured, and thus the discharge current could be determined. Experiments with variable DC bias were also carried out. The bias voltage was generated using a robust DC voltage generator with near-zero resistance, and it was applied to the substrate holder isolated from the grounded chamber walls. The bias current was measured with an ammeter.

The atomic composition of the films was measured through energy dispersive spectroscopy (EDS) using a Scios 2 dual beam scanning electron microscope equipped with an X-Max 20 EDX detector (Oxford Instruments, Abingdon, Oxfordshire, UK). For the measurements, an electron beam of 4.2 keV energy and 3.2 nA current was used. The evaluation of the spectra was performed using Aztec software, version 5.0 provided for the

detector. The calibration of the instrument was performed with factory standards of  $\text{Al}_2\text{O}_3$  and  $\text{SiO}_2$  for the elements of Al and O, respectively. Apart from O and Al, C and Si (coming from the substrate) were also detected for the determination of the layers' composition; the latter were deconvoluted from the spectra.

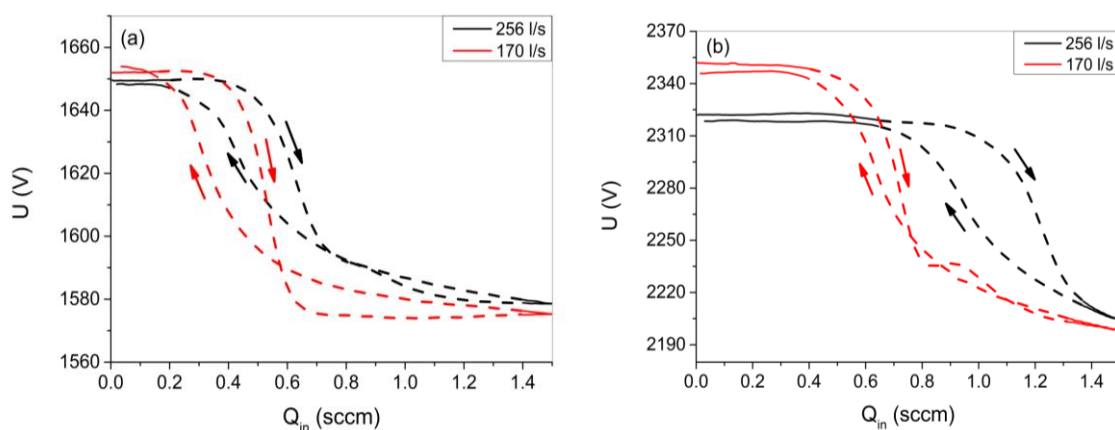
### 3. Results

Table 1 presents the O/Al atomic concentration ratio for layers sputtered with different oxygen flow rates ( $Q_{in}$ ) (the EDS spectra can be found in the Supplementary information file). It can be seen that a composition close to the ideal stoichiometry (i.e., O/Al atomic concentration ratio = 3/2) was only achieved for the layers that were deposited at higher  $Q_{in}$  (1.5 and 2 sccm). Applying a substrate bias of  $-100$  V did not noticeably change the composition of the layers.

**Table 1.** The O/Al atomic concentration ratio measured through EDS for alumina layers prepared through reactive sputtering using different oxygen flow rates and a constant target current of  $I = 123$  mA. The RF power was between 212 and 234 W.

$Q_{in}$ (sccm)	O/Al at. Conc. Ratio
0.5	24/76
0.75	42/58
1.5	57/43
2	57/43

Figure 1 shows the measured target voltage data as a function of the oxygen flow rate. It is evident from the figure that there is a marked difference in the voltage data for increasing and decreasing gas flow rate, indicating hysteresis behavior (shown by a dotted line). It is also seen that the use of greater RF power shifts the hysteresis curve to higher flow rates, while the decrease of the pumping speed shifts it to lower  $Q_{in}$ . Note that there is anomalous behavior at higher flow rates, i.e., crossing of the hysteresis curves. This can be attributed to the operation of the RF generator and the associated manual matching circuit. As target coverage increases, reflected RF power appears, indicating slight detuning of the matching, which effectively reduced the power delivered to the target.



**Figure 1.** Hysteresis curves of the measured target voltage as a function of the oxygen flow at an RF power of 150 W (a) and 300 W (b) for different pumping speeds.

#### 3.1. Modeling the Reactive Sputtering Process

The Berg model was utilized to model the reactive sputtering. Our approach employs the flow rate and the variable pumping speed of the turbomolecular pump as independent variables in the equations that describe the sputtering process. The classical Berg model

is utilized due to the fact that the magnetron-less RF sputtering device is operated at a relatively low power; thus, the ion currents are not excessively high. Under these conditions, the ion implantation effects on the target surface are expected to be relatively small. Therefore, by using the classical Berg model [2], ion implantation effects on the target were neglected. The reactive gas flow balance based on the Berg model can be written as follows:

$$Q_{in} = \frac{ps}{k_B T} + \alpha_t F(1 - \theta_t)A_t + \alpha_s F(1 - \theta_s)A_s, \quad (1)$$

where  $Q_{in}$  is the reactive gas flow rate,  $p$  is the reactive gas pressure,  $s$  is the pumping speed for the reactive gas,  $k_B$  is the Boltzmann constant,  $T$  is the temperature inside of the sputtering chamber, and  $\alpha_t$  and  $\alpha_s$  are the sticking coefficients of the target and the substrate, respectively.  $A_t$  and  $A_s$  are the surface area of the target and the collecting area (approximately the area of the substrate holder), respectively, and  $\theta_t$  and  $\theta_s$  are the surface coverage of the target and the substrate, respectively. The flux of reactive gas molecules ( $F$ ) can be given as

$$F = \frac{p}{\sqrt{2\pi k_B T m}}, \quad (2)$$

where  $m$  is the mass of the reactive gas molecule.

The surface coverage of the target and the substrate in the case of alumina deposition and oxygen as reactive gas can be written as

$$\theta_t = \frac{\frac{2}{z}a_t F}{\frac{J}{e}Y_c + \frac{2}{z}a_t F}, \quad (3)$$

$$\theta_s = \frac{\frac{J}{e}Y_c \theta_t A_t + \frac{2}{z}a_s F A_s}{\frac{J}{e}Y_m(1 - \theta_t)A_t + \frac{J}{e}Y_c \theta_t A_t + \frac{2}{z}a_s F A_s}, \quad (4)$$

where  $J$  is the ion current density of the target,  $z$  represents the compound stoichiometry ( $z = 1.5$  for  $\text{Al}_2\text{O}_3$ ),  $e$  is the elementary charge, and  $Y_m$  and  $Y_c$  are the sputtering yield of Al and  $\text{Al}_2\text{O}_3$ , respectively.

To simplify the equations, the following dimensionless parameters (see also Appendix A) are introduced, as in [5],

$$A_r = \frac{A_s}{A_t}, X = \frac{1}{Y_c}, r_y = \frac{Y_c}{Y_m}, S = \frac{s}{A_t} \sqrt{\frac{2\pi m}{k_B T}}, P = \frac{F}{J/e} = \frac{p}{(J/e)\sqrt{2\pi k_B T m}}, \quad (5)$$

along with the parameter  $\tau = \frac{e}{JA_t}$  with the dimension of seconds.

With these quantities, the surface coverages can be written as

$$1 - \theta_t = \frac{1}{\frac{2}{z}\alpha_t P X + 1}, \quad (6)$$

$$1 - \theta_s = \frac{1}{1 + r_y \left( \frac{2}{z}\alpha_t P X + \frac{2}{z}\alpha_s P X A_r \left( \frac{2}{z}\alpha_t P X + 1 \right) \right)}. \quad (7)$$

Equation (1) takes the form of

$$Q_{in} = \frac{P}{\tau} \left[ S + \frac{\frac{2}{z}\alpha_t}{\frac{2}{z}\alpha_t P X + 1} + \frac{\frac{2}{z}\alpha_s A_r}{1 + r_y \left( \frac{2}{z}\alpha_t P X + \frac{2}{z}\alpha_s P X A_r \left( \frac{2}{z}\alpha_t P X + 1 \right) \right)} \right]. \quad (8)$$

It is already known from Berg's original article that the condition for the existence of hysteresis is that the increase in the reactive gas pressure should be accompanied by a decrease in the reactive flow, i.e., the gas flow curve has a negative slope at some pressure.

In order to determine the boundaries of the hysteresis region, the derivative of Equation (8) is formed, and the zero points of this function are identified.

$$\frac{\partial Q_{in}\tau}{\partial P} = \left[ S + \frac{\frac{2}{z}\alpha_t}{(c_1P + 1)^2} + \frac{y_0^2c_2 - c_2c_1^2P^2}{y_0^2(M)^2} \right] = 0. \quad (9)$$

Here, the following notation was used:

$$c_1 \equiv \frac{2}{z}\alpha_t X, \quad c_2 \equiv \frac{2}{z}\alpha_s A_r, \quad y_0^2 \equiv \frac{\frac{2}{z}\alpha_t}{r_y c_2}, \quad M \equiv 1 + r_y \left( \frac{2}{z}\alpha_t P X + \frac{2}{z}\alpha_s P X A_r \left( \frac{2}{z}\alpha_t P X + 1 \right) \right). \quad (10)$$

The solution to Equation (9) for  $P$  as an unknown quantity enables the determination of the values of the data points at which  $dQ_{in}/dP$  assumes negative values. A detailed description of this procedure, employing numerical methods, can be found in ref. [3]. Unfortunately, Equation (9) is a sixth-degree equation in  $P$ , and there is currently no explicit analytical solution. However, there is an illustrative option that implicitly suggests a solution. This is promising because the derivation of the quotients in the equation also means squaring the denominators. Taking this into account,  $\theta_t$  and  $\theta_s$  can be substituted into Equation (9):

$$\frac{\partial Q_{in}\tau}{\partial P} = \left[ S + \frac{2}{z}\alpha_t (1 - \theta_t)^2 + (1 - \theta_s)^2 (c_2 - c_2 \frac{c_1^2}{y_0^2} P^2) \right]. \quad (11)$$

Equating this equation to zero, we can determine the pressure (sometimes called critical pressure) from which a small deviation leads to the unstable region. It is important to emphasize that if the basic equation (Equation (9)) does not have a solution, the process is hysteresis-free. Two interesting things are worth noting in connection with this equation. One is that all variable and changeable technical and material parameters are included—although implicitly—in a single equation. Consequently, the system's status can be displayed directly after the parameters have been mapped. The other thing to note is that the only term that can make the derivative function negative is the 3rd term in Equation (9), which is related to the number of oxygen molecules forming a compound on the collector's surface (i.e., the substrate and the chamber walls). Equating Equation (11) to zero, we obtain a quadratic expression:

$$P^2 = y_0^2 \frac{\left[ S + \frac{2}{z}\alpha_t (1 - \theta_t)^2 \right]}{c_1^2 (1 - \theta_s)^2} + \frac{y_0^2}{c_1^2}. \quad (12)$$

Based on this, a  $P_{min}$  value can be given, which can be regarded as the lower estimate of the boundary of the hysteresis region:

$$P_{min}^2 = \frac{y_0^2}{c_1^2}. \quad (13)$$

It is perhaps surprising, but certainly an important finding for the technology comes from the solution of Equation (11) after substituting Equation (6) back,

$$S(c_1P + 1)^2 + \frac{2}{z}\alpha_t + (c_1P + 1)^2(1 - \theta_s)^2 \left( c_2 - c_2 \frac{c_1^2}{y_0^2} P^2 \right) = 0, \quad (14)$$

if we choose the realistic coverage parameter  $\theta_s = 1$ , i.e., depositing a stoichiometric layer. In this case, the equation takes the form of  $S(c_1P + 1)^2 = -\frac{2}{z}\alpha_t$ , i.e., there is no root of the basic equation. It is hypothesized that the technological process, which successfully

deposits the stoichiometric layer, is effective at avoiding the risk of process instability caused by hysteresis.

The goal of most technological processes is to deposit a stoichiometric layer. In accordance with the established mathematical formula, it can be concluded that the quantity  $M$  assumes a large value. It gives an opportunity for further simplification, opening up the possibility of an analytical solution to the basic equation. After some manipulation, we can transform  $M$  into a product. We can use that  $M \gg 1$  in a stoichiometric layer deposition:

$$(c_1P + 1)(c_1P) = \frac{M - 1 - r_y c_1P}{\frac{1}{y_0^2}} \approx My_0^2, \quad (15)$$

By using this approximation, Equation (9) takes the form of

$$S(c_1P + 1)^2(c_1P)^2 - \left[ \frac{2\alpha_t}{r_y}(1 - r_y) \right] (c_1P)^2 + c_2y_0^4 = 0. \quad (16)$$

An additional rough approximation can greatly simplify the direct analytical solution of this equation,

$$(c_1P + 1)^2(c_1P)^2 \approx (c_1P)^4, \quad (17)$$

which gives us the following expression:

$$S(c_1P)^4 - \left[ \frac{2\alpha_t}{z r_y}(1 - r_y) \right] (c_1P)^2 + c_2y_0^4 = 0. \quad (18)$$

The solutions of this equation are provided by the solving formula for quadratic equations. It is worthwhile to calculate the zero value of the determinant that defines the only root (denoted by  $*$ ) of Equation (18). This directly determines an  $S^*$  value, which is required for a unique solution to exist:

$$S^* = \frac{c_2}{4}(1 - r_y)^2. \quad (19)$$

In this case, the  $P^*$  root has the form of

$$(c_1P^*)^2 = \frac{2y_0^2}{1 - r_y}. \quad (20)$$

which is approximately twice as much as  $(c_1P_{min})^2 = y_0^2$ .

In the following, an analytical solution using the standard solution formula for Equation (18) is given to estimate the range of hysteresis (with the simplification of  $\sqrt{1-x} \approx 1 - x/2$ ). We obtain two solutions,  $P_1$  and  $P_2$ , for  $S < S^*$ :

$$(c_1P_1)^2 = c_2y_0^2 \left( \frac{(1 - r_y)}{S} - \frac{1}{c_2(1 - r_y)} \right), \quad (21)$$

$$(c_1P_2)^2 = y_0^2 = (c_1P_{min})^2. \quad (22)$$

The latter is also equal to Equation (13).

The boundaries of the hysteresis region, also called critical pressures ( $P_{crit}$ ), determined numerically as well as analytically (i.e.,  $P_1$  and  $P_2$ ) as a function of the pumping speed ( $S$ ), are illustrated in Figure 2. While the first critical pressure slightly increases, the second critical pressure significantly decreases with the increase of the pumping speed. As a result, at higher pumping speeds, the region of hysteresis narrows, and the region above the upper boundary of hysteresis can be reached at lower pressures, in agreement with refs. [2,12].

$P_{min}$  (Equation (13)) and  $P^*$  (Equation (20)) are also highlighted in the figure. These points and the curve determined through Equation (21) can be used to identify the area where the equation defining hysteresis has an analytical solution; we have marked them in Figure 2 with red lines. The value of  $S^*$  appears to be an overestimate compared to the simulated value; this is because our approximation is more accurate for large  $P$  values.

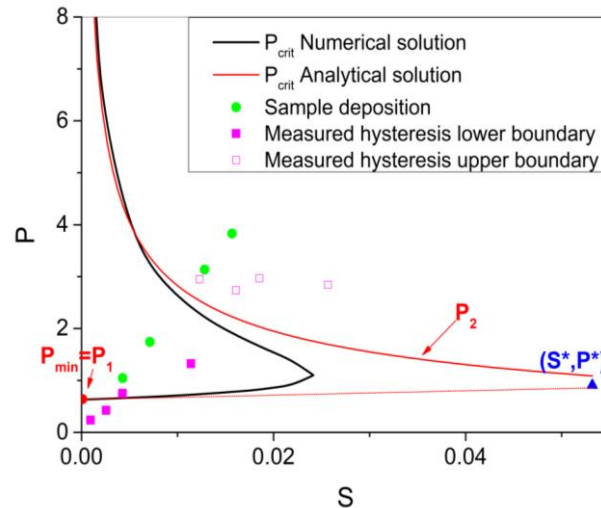


**Figure 2.** Dimensionless pressure versus dimensionless pumping speed stability state diagram. The critical pressures calculated numerically based on Equation (9) are presented as black lines, and the analytic solutions, as presented in Equations (21) and (22), are shown as red curves. In the region surrounded by these curves, the system exhibits hysteresis behavior. The points of the actual deposition experiments and the experimentally determined boundary of hysteresis curves are also highlighted.

It is interesting to note that  $y_0^2$  is a fundamental parameter of the equation. Among other things, its value is proportional to  $\alpha_t/\alpha_s$ . While the  $\alpha_t$  and  $\alpha_s$  sticking coefficient values obviously depend on the temperature [17,18], we can assume that their ratio does not depend on it or only slightly depends on it. It is worth examining the first term in Equation (1); this is the number of  $O_2$  molecules that must be removed from the system to achieve stable operation (in the absence of hysteresis). After making the necessary substitutions, we obtain  $p^*s^*/k_B T \propto (\alpha_t/\alpha_s)^{1/2}$ . This can be interpreted as meaning that in the case of higher target temperature, the number of molecules to be removed must be increased for stability. If a heated substrate is used, on the contrary, the amount of reactive gas to be removed must be reduced. This indication is of course valid if the temperature  $T$  of the gas mixture in the chamber is considered constant.

Figure 2 shows the hysteresis state diagram for a layer deposited using a target and a single reactive gas; the points suggested by Equations (21) and (22) are easy to plot. In the case of sputtering with two targets in the same gas space (co-sputtering), it is worth plotting the state diagram in a similar manner, because in this way the optimum deposition conditions can be set by the DC voltage or RF power applied to the targets with appropriate sizes. The sputtering technology may involve the deposition of a compound material, such as oxynitride. In this case, the phase diagram of both reactive gases can be plotted in the same coordinate system. The study of this plot can assist in selecting the appropriate partial pressures and electrical power applied to the target.

### 3.2. Effect of Bias

Negative bias on the substrate during DC and RF sputtering is usually applied to modify the direction and kinetic energy of the arriving particles to the substrate surface. This can improve the physical properties of the layer, such as the resistance, morphology, or

surface roughness [19–21]. By controlling the direction and kinetic energy of the particles, greater penetration into the substrate’s surface can be achieved, resulting in better adhesion. On the other hand, bombarding the surface of the deposited film with particles of sufficient energy can cause re-sputtering of the deposited layer. We would like to point out that morphological studies are not the subject of this work; the description of the material parameters of the deposited layer will be published elsewhere.

The negative bias is most simply generated by grounding the plasma current through an impedance on the substrate holder isolated from the chamber. In this case, the applied impedance, the so-called value of the self-bias, determines the value of the resulting voltage. However, an arbitrary bias can also be created if a DC voltage generator with negligible internal resistance is connected between the substrate holder and the grounded plate of the chamber. This arrangement is essentially similar to the Langmuir test or the Sobolewsky test [22–24]. In the course of our work, the DC bias current  $I_m$  was measured, and it is illustrated in Figure 3.

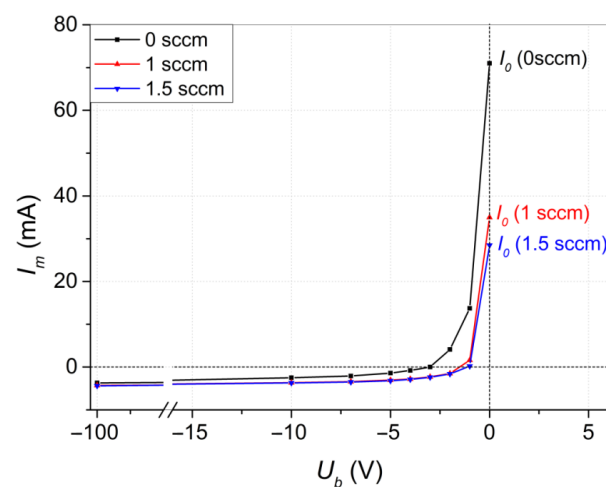


**Figure 3.** Measured bias current as a function of the bias voltage in the case of sputtering of an Al target for different oxygen flow rates. At zero bias voltage (i.e., at the short circuit), the measured  $I_m$  value is denoted by  $I_0$ .

At a negative potential, the probe attracts positive ions and repels electrons, as a result of which the ion current makes up the large part of the probe current. However, some electrons may have sufficiently high energy to overcome the probe potential. By increasing the potential, we reach a point where the charge of ions and electrons is in balance. In this case, the probe current is zero, and the potential  $U_0$  is the “floating potential”, using the plasma physics term. In the following, we only consider the  $U_B < U_0$  values when modifying the equations.

The physical conditions of the negatively biased substrate can be imagined as similar to those of the target. Consequently, the biased substrate also satisfies the role of a negatively charged target, which is sputtered with the discharge current  $I' = (I_0 - I_m)$ , where  $I_m$  is the DC bias current measured with an ammeter (its value is positive for  $U_B < U_0$ , as  $I_m$  takes on negative values). According to our explanation, the effect of the bias voltage can be interpreted by the  $J'$  ion current density ( $J' = I'/A_c$ ) generated compared to the short-circuited state, where  $A_c$  is the biased part of the collecting area. After complementing the Berg model with the introduction of  $J'$ , it is possible to separate the values of  $\theta_t$  and  $\theta_c$ , which are determined through the model (Equation (1)). Based on this approach, with the traditional notation of the Berg equations [2], the balances of the target and the biased part of the substrate ( $A_c$ ) can be written as follows (schematically depicted in Figure 4):

$$F_c + F'_m \theta_t = \frac{2}{z_t} \alpha F(1 - \theta_t) A_t + F'_c(1 - \theta_t), \tag{23}$$

$$\frac{2}{z_s} \alpha F(1 - \theta_c) A_s + F_c(1 - \theta_c) = \theta_c F_m + F'_c, \tag{24}$$

where  $\theta_c$  indicates the surface coverage of the biased part of the collecting area and  $A_s$  is the full collecting area.

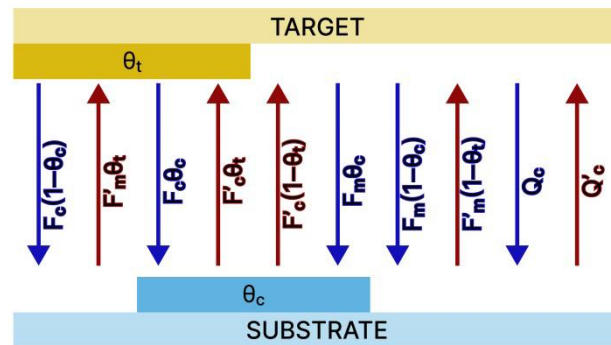


**Figure 4.** Schematic representation of the material fluxes during sputtering in the case of negative substrate bias.

The material fluxes are defined as

$$F_c = \frac{J}{e} Y_c \theta_t A_t, F_m = \frac{J}{e} Y_m (1 - \theta_t) A_t, \tag{25}$$

$$F'_c = \frac{J'}{e} Y_c \theta_c A_c, F'_m = \frac{J'}{e} Y_m (1 - \theta_c) A_c. \tag{26}$$

It is worthwhile to return to the previously introduced dimensionless quantities.

$$Y_c \theta_t A_t + \frac{J'}{J} Y_m (1 - \theta_c) A_c \theta_t = \frac{2}{z_t} \alpha P(1 - \theta_t) A_t + \frac{J'}{J} Y_c \theta_c A_c (1 - \theta_t), \tag{27}$$

$$\frac{2}{z_s} \alpha P A_s (1 - \theta_c) + Y_c \theta_t A_t (1 - \theta_c) = Y_m A_t (1 - \theta_t) \theta_c + \frac{J'}{J} Y_c \theta_c A_c. \tag{28}$$

By further transforming these equations, we obtain

$$r_y \theta_t + \frac{J'}{J} A_b (1 - \theta_c) \theta_t = r_y \frac{2}{z_t} \alpha P X (1 - \theta_t) + \frac{J'}{J} A_b r_y (1 - \theta_t) \theta_c, \tag{29}$$

$$\frac{2}{z_s} \alpha_s r_y X P A_r (1 - \theta_c) + r_y \theta_t (1 - \theta_c) = (1 - \theta_t) \theta_c + \frac{J'}{J} A_b r_y \theta_c, \tag{30}$$

where  $A_b = \frac{A_c}{A_t}$  and  $A_r = \frac{A_s}{A_t}$ . The  $\theta_t$  and  $\theta_c$  quantities can be easily expressed from the equations if we perform a series expansion according to  $J'$ ,

$$\theta_{t,c} = \theta_{t,c}^0 + J' \frac{\partial \theta_{t,c}^0}{\partial J'}, \tag{31}$$

where  $\theta_{t,c}^0 \equiv \theta_{t,c}(J' = 0)$ , i.e., Equations (6) and (7).

After the series expansion, the surface coverages can be expressed as

$$\theta_c = \theta_c^0 \left[ 1 - \frac{J'}{J} \frac{r_y A_b}{r_y A_r \frac{2}{z_s} \alpha_s P X + r_y \theta_t^0 + 1 - \theta_t^0} \right], \tag{32}$$

$$\theta_t = \theta_t^0 \left[ 1 - \frac{J'}{J} A_b \frac{\theta_t^0 (1 - \theta_c^0) - \theta_c^0 r_y (1 - \theta_t^0)}{r_y \frac{2}{z} \alpha_t P X} \right]. \quad (33)$$

Figure 5 shows the coverage of the substrate and the target as a function of oxygen partial pressure for different bias current/target current density ratios, calculated from Equations (32) and (33). The substrate coverage is practically unchanged when a bias is applied compared to the unbiased case (the plotted curves are on top of each other). In contrast, the target coverage can be significantly changed at lower pressures by using a substrate bias, i.e., one needs higher oxygen pressure to obtain the same target state.

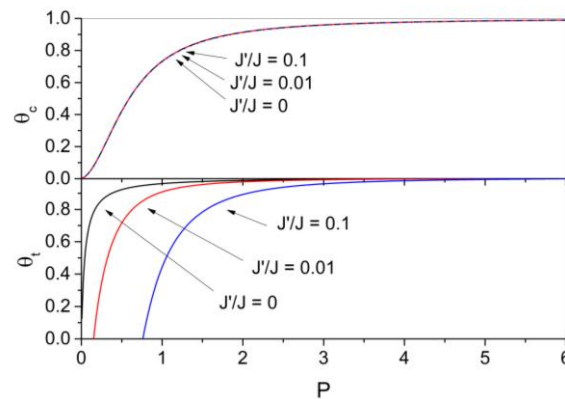


**Figure 5.** Calculated target (lower panel) and substrate (upper panel) coverage as a function of the dimensionless pressure for different current density ratios ( $J'/J$ ).

The result can be explained by the fact that by applying a bias on the substrate, electrons are accelerated by the potential difference between the biased substrate holder and the grounded collector surfaces, and this contributes to the increase in ionization of the gas in the vicinity of the substrate. The change in the target state can be attributed to the deposition of atoms from the substrate onto the target. Due to the higher sputtering yield of metal, compared to the oxide, redeposition from the substrate is dominated by the metal atoms, thereby resulting in a more metallic surface of the target.

It is easy to verify that  $\theta_c$  does not change under bias; we repeated the deposition of alumina layers with similar parameters but with a bias of 100 V. EDS measurements showed no significant change in the atomic ratios compared to the unbiased case. Conversely, we cannot directly verify the change in  $\theta_t$  through measurement, as the sensitivity of the single vacuum gauge is not sufficient to detect the change in oxygen partial pressure. There is an indirect solution to monitor the change in the oxidation state of the target  $\theta_t$ . This is based on the fact that the secondary emission of the oxide coating is higher than that of the metallic target [10]. The change in current is inversely proportional to the change in voltage created on the target, as the RF generator delivers constant power into 50  $\Omega$ . The relative oxidation state of the target can be defined as the ratio between the target voltage change  $\Delta V$  (between the unbiased and biased cases) for a given oxygen flow (Figure 6a) and the voltage difference in the metallic and oxidized states of the target (see ref. [13]), as shown in the Figure 6b. The voltage difference is negligible for large  $P$ , while it gradually increases as the pressure is decreased. The measurement seems to confirm the result of the calculation.

The effect of bias on the physical properties of the deposited layer is not the focus of this study. It is argued that a suitably chosen DC bias voltage serves as a continuous tuning possibility for the  $\theta_t$  separated from  $\theta_c$ . This can be used, for example, in cases where the target is prone to arcing due to poisoning.

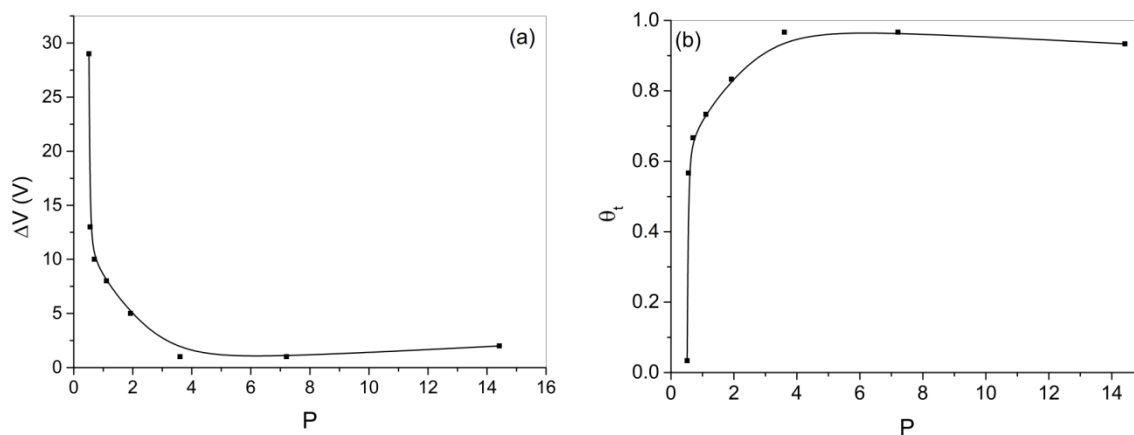


**Figure 6.** The difference between the target voltages ( $\Delta V$ ) when using an unbiased and a biased ( $-100$  V) substrate (a) and the oxidation state of the target ( $\theta_t$ ) (b) as a function of the dimensionless pressure.

#### 4. Conclusions

In this study, we presented the numerical and approximate analytical solutions of the equations that describe the reactive sputtering process based on the Berg model. A stability state diagram was constructed. The relatively simple analytical solution was shown to be a good approximation of the numerical solution. While the analytical solution of the equation was given as a function of the pressure of the reactive gas, the discharge current, and the pumping speed, the basic equation also allows for the examination of all other parameters. In examples of sputtering involving two targets within a single gas space or the deposition of a composite material employing two reactive components, it would be advantageous to plot the state diagram within the same coordinate system. This approach ensures that the most favorable deposition conditions can be selected by the experimentalist who is already familiar with reactive sputtering technology.

It was also demonstrated that a direct current (DC) substrate bias can be employed as a continuous tuning mechanism for target coverage by compound molecules  $\theta_t$  separated from the substrate coverage  $\theta_c$ . This can be helpful in certain cases where the arcing of the target makes process control difficult.

**Supplementary Materials:** The following supporting information can be downloaded at <https://www.mdpi.com/article/10.3390/coatings15050499/s1>.

**Author Contributions:** Conceptualization, M.S.; methodology, M.S. and N.H.; formal analysis, M.S. and M.G.; investigation, D.O. and M.S.; writing—original draft preparation, M.S. and M.G.; writing—review and editing, M.G.; visualization, M.G. All authors have read and agreed to the published version of the manuscript.

**Funding:** Project no. C1792954 has been implemented with the support provided by the Ministry of Culture and Innovation of Hungary from the National Research, Development and Innovation Fund, financed under the KDP-2021 funding scheme. The funding provided by the Hungarian Scientific Research Fund OTKA, grant number K143216, is gratefully acknowledged.

**Institutional Review Board Statement:** Not applicable.

**Informed Consent Statement:** Not applicable.

**Data Availability Statement:** Data are contained within the article and the Supplementary Materials.

**Acknowledgments:** The authors are thankful to György Sáfrán and Noémi Szász for their support of this work.

**Conflicts of Interest:** The following authors declare no conflicts of interest: M. Gajdics, D. Olasz, and M. Serényi. N. Hegedűs discloses that she is employed by Guardian Orosháza Ltd.; however, her contributions to this manuscript were made independently without any requirement, guidance, or input by her employer. She also discloses that she received no financial compensation from any source for her contribution. The funders had no role in the design of the study; in the collection, analyses, or interpretation of data; in the writing of the manuscript; or in the decision to publish the results.

## Appendix A

Table A1 shows the parameters used in this study. For the sticking coefficient, the value given in ref. [25] was used. The yield parameters were determined by fitting the  $\theta_s$  (calculated based on the EDS measurement) as a function of  $F$ , as presented in Equation (4), with the yield parameters as variables. The  $A_t$  and the  $A_s$  were 44 cm<sup>2</sup> and 66 cm<sup>2</sup>, respectively; hence,  $A_r$  was calculated as 1.5. The  $P$  and  $S$  ranges in which the sputtering experiments were performed are also given. Table A2 lists all of the symbols used in this study and their meaning.

**Table A1.** The dimensionless parameters used in this study.

$\alpha_t = \alpha_s$	0.107
$Y_m$	2.09
$Y_c$	0.006
$X$	166
$r_y$	0.003
$A_r$	1.5
$P$	1–3.8
$S$	0.004–0.016

**Table A2.** List of symbols used in this study in the order of their occurrence.

Symbol	Meaning
$Q_{in}$	Oxygen flow rate
$p$	Oxygen partial pressure
$s$	Pumping speed for the reactive gas
$k_B$	Boltzmann constant
$T$	Temperature inside of the chamber
$\alpha_t$	Sticking coefficient on the target
$\alpha_s$	Sticking coefficient on the substrate
$A_t$	Surface area of the target
$A_s$	Collecting area
$\theta_t$	Surface coverage of the target
$\theta_s$	Surface coverage of the substrate
$F$	Reactive gas flux
$m$	Mass of the reactive gas molecule
$J$	Ion current density of the target
$z$	Stoichiometry ratio
$e$	Elementary charge
$Y_m$	Sputtering yield of the metal
$Y_c$	Sputtering yield of the compound

Table A2. Cont.

Symbol	Meaning
$A_r$	Surface area ratio (Equation (5))
$X$	$1/Y_c$ (Equation (5))
$r_y$	Sputtering yield ratio (Equation (5))
$S$	Dimensionless pumping speed (Equation (5))
$P$	Dimensionless pressure (Equation (5))
$\tau$	$e/JA_t$ (Equation (5))
$c_1$	$2\alpha_t X/z$ (Equation (10))
$c_2$	$2\alpha_s A_r/z$ (Equation (10))
$y_0^2$	$2\alpha_t/(zr_y c_2)$ (Equation (10))
$M$	$1 + r_y (2\alpha_t PX/z + 2\alpha_s PXA_r/z (2\alpha_t PX/z + 1))$ (Equation (10))
$P_{min}$	Lower estimate of the boundary of the hysteresis region
$S^*$	Dimensionless pumping speed for which only one solution of Equation (18) exists
$P^*$	Root of Equation (18) for $S = S^*$ (critical pressure)
$P_1$ and $P_2$	Solutions of Equation (18) for $S < S^*$ (critical pressures)
$I_m$	DC bias current
$I_0$	Bias current measured at the short circuit
$U_b$	Substrate bias voltage
$I'$	Ion current at the substrate
$J'$	Ion current density at the substrate
$\Delta V$	Difference between the target voltages ( $\Delta V$ ) when using an unbiased and a biased substrate

## References

- Kadlec, S.; Musil, J.; Vyskocil, H. Hysteresis Effect in Reactive Sputtering: A Problem of System Stability. *J. Phys. D Appl. Phys.* **1986**, *19*, L187. [\[CrossRef\]](#)
- Berg, S.; Nyberg, T. Fundamental Understanding and Modeling of Reactive Sputtering Processes. *Thin Solid Film.* **2005**, *476*, 215–230. [\[CrossRef\]](#)
- Strijckmans, K.; Schelfhout, R.; Depla, D. Tutorial: Hysteresis during the Reactive Magnetron Sputtering Process. *J. Appl. Phys.* **2018**, *124*, 241101. [\[CrossRef\]](#)
- Berg, S.; Särhammar, E.; Nyberg, T. Upgrading the “Berg-Model” for Reactive Sputtering Processes. *Thin Solid Film.* **2014**, *565*, 186–192. [\[CrossRef\]](#)
- Li, C.; Hsieh, J.-H. Stability Analysis of Reactive Sputtering Process with Variable Sticking Coefficients. *Thin Solid Film.* **2005**, *475*, 102–108. [\[CrossRef\]](#)
- Depla, D.; Heirwegh, S.; Mahieu, S.; De Gryse, R. Towards a More Complete Model for Reactive Magnetron Sputtering. *J. Phys. D Appl. Phys.* **2007**, *40*, 1957. [\[CrossRef\]](#)
- Strijckmans, K.; Leroy, W.P.; De Gryse, R.; Depla, D. Modeling Reactive Magnetron Sputtering: Fixing the Parameter Set. *Surf. Coat. Technol.* **2012**, *206*, 3666–3675. [\[CrossRef\]](#)
- Bartzsch, H.; Frach, P. Modeling the Stability of Reactive Sputtering Processes. *Surf. Coat. Technol.* **2001**, *142–144*, 192–200. [\[CrossRef\]](#)
- Särhammar, E.; Strijckmans, K.; Nyberg, T.; Van Steenberge, S.; Berg, S.; Depla, D. A Study of the Process Pressure Influence in Reactive Sputtering Aiming at Hysteresis Elimination. *Surf. Coat. Technol.* **2013**, *232*, 357–361. [\[CrossRef\]](#)
- Depla, D.; Mahieu, S.; De Gryse, R. Magnetron Sputter Deposition: Linking Discharge Voltage with Target Properties. *Thin Solid Film.* **2009**, *517*, 2825–2839. [\[CrossRef\]](#)
- Wang, Q.; Fang, L.; Liu, Q.; Chen, L.; Wang, Q.; Meng, X.; Xiao, H. Target Voltage Hysteresis Behavior and Control Point in the Preparation of Aluminum Oxide Thin Films by Medium Frequency Reactive Magnetron Sputtering. *Coatings* **2018**, *8*, 146. [\[CrossRef\]](#)
- Musil, J.; Baroch, P.; Vlček, J.; Nam, K.H.; Han, J.G. Reactive Magnetron Sputtering of Thin Films: Present Status and Trends. *Thin Solid Film.* **2005**, *475*, 208–218. [\[CrossRef\]](#)
- van Emmerik, C.I.; Hendriks, W.A.P.M.; Stok, M.M.; de Goede, M.; Chang, L.; Dijkstra, M.; Segerink, F.; Post, D.; Keim, E.G.; Dijkers, M.J.; et al. Relative Oxidation State of the Target as Guideline for Depositing Optical Quality RF Reactive Magnetron Sputtered Al<sub>2</sub>O<sub>3</sub> Layers. *Opt. Mater. Express OME* **2020**, *10*, 1451–1462. [\[CrossRef\]](#)

14. Stauder, B.; Perry, F.; Frantz, C. Chemical and Structural Analysis of Aluminium-Oxygen Coatings Obtained by d.c. Magnetron Reactive Sputtering: Some Features of the Process. *Surf. Coat. Technol.* **1995**, *74–75*, 320–325. [[CrossRef](#)]
15. Koski, K.; Hölsä, J.; Juliet, P. Deposition of Aluminium Oxide Thin Films by Reactive Magnetron Sputtering. *Surf. Coat. Technol.* **1999**, *116–119*, 716–720. [[CrossRef](#)]
16. Chiba, Y.; Abe, Y.; Kawamura, M.; Sasaki, K. Effects of Total Gas Flow Rate and Sputtering Power on the Critical Condition for Target Mode Transition in Al–O<sub>2</sub> Reactive Sputtering. *Vacuum* **2009**, *84*, 629–632. [[CrossRef](#)]
17. Rose, M.; Bartha, J.W.; Endler, I. Temperature Dependence of the Sticking Coefficient in Atomic Layer Deposition. *Appl. Surf. Sci.* **2010**, *256*, 3778–3782. [[CrossRef](#)]
18. Asnin, L.D.; Chekryshkin, Y.S.; Fedorov, A.A. Calculation of the Sticking Coefficient in the Case of the Linear Adsorption Isotherm. *Russ. Chem. Bull.* **2003**, *52*, 2747–2749. [[CrossRef](#)]
19. Choi, D. The Critical Role of Substrate Bias for the Sputter Deposition of Molybdenum Thin Films. *Microelectron. Eng.* **2019**, *216*, 111084. [[CrossRef](#)]
20. Khánh, N.Q.; Radó, J.; Horváth, Z.E.; Soleimani, S.; Oyunbolor, B.; Volk, J. The Effect of Substrate Bias on the Piezoelectric Properties of Pulse DC Magnetron Sputtered AlN Thin Films. *J. Mater. Sci. Mater. Electron.* **2020**, *31*, 22833–22843. [[CrossRef](#)]
21. Yang, Z.-H.; Wu, P.-C.; Chuang, T.-H. Effects of Substrate Bias on the Sputtering of High Density (111)-Nanotwinned Cu Films on SiC Chips. *Sci. Rep.* **2022**, *12*, 15408. [[CrossRef](#)] [[PubMed](#)]
22. Sobolewski, M.A. Measuring the Ion Current in Electrical Discharges Using Radio-Frequency Current and Voltage Measurements. *Appl. Phys. Lett.* **1998**, *72*, 1146–1148. [[CrossRef](#)]
23. Sobolewski, M.A. Sheath Model for Radio-Frequency-Biased, High-Density Plasmas Valid for All  $\omega/\omega_1$ . *Phys. Rev. E* **2000**, *62*, 8540–8553. [[CrossRef](#)] [[PubMed](#)]
24. Sezemsky, P.; Stranak, V.; Kratochvil, J.; Cada, M.; Hippler, R.; Hrabovsky, M.; Hubicka, Z. Modified High Frequency Probe Approach for Diagnostics of Highly Reactive Plasma. *Plasma Sources Sci. Technol.* **2019**, *28*, 115009. [[CrossRef](#)]
25. Leroy, W.P.; Mahieu, S.; Persoons, R.; Depla, D. Quantification of the Incorporation Coefficient of a Reactive Gas on a Metallic Film during Magnetron Sputtering: The Method and Results. *Thin Solid Film.* **2009**, *518*, 1527–1531. [[CrossRef](#)]

**Disclaimer/Publisher’s Note:** The statements, opinions and data contained in all publications are solely those of the individual author(s) and contributor(s) and not of MDPI and/or the editor(s). MDPI and/or the editor(s) disclaim responsibility for any injury to people or property resulting from any ideas, methods, instructions or products referred to in the content.